International Journal of Solids and Structures 217–218 (2021) 74–89

Contents lists available at ScienceDirect

International Journal of Solids and Structures

journal homepage: www.elsevier.com/locate/ijsolstr

Modeling of cracks in two-dimensional elastic bodies by coupling the boundary element method with peridynamics

Yang Yang *, Yijun Liu *

Department of Mechanics and Aerospace Engineering, Southern University of Science and Technology, Shenzhen, China

ARTICLE INFO

Article history:
Received 16 September 2020
Received in revised form 25 January 2021
Accepted 2 February 2021
Available online 11 February 2021

Keywords:
Multi-scale method
Boundary element method
Peridynamics
Crack propagation

ABSTRACT

A multi-scale method based on a combination of the boundary element method (BEM) and peridynamics (PD) was developed to model crack propagation problems in two-dimensional (2D) elastic bodies. The special feature of this method is that it can take full advantage of both the BEM and PD to achieve a higher level of computational efficiency. Based on the scale of the structure and the crack location, the considered domain can be divided into non-cracked and cracked domains. The BEM is employed in the non-cracked domain, while the PD is applied in the cracked domain. This can reduce the dimension by one in the non-cracked domain for improving the modeling efficiency. A stiffness equation of the bond-based PD is established by using Taylor's series expansion for the bond stretch and applied to simulate the cracked domain. The PD approach can automatically model the initiation and propagation of a crack. A coupling model using shared nodes is constructed by introducing the BEM nodes on the interface at the same location as the PD material points. With the continuity of displacements and equilibrium of tractions at the interface, a combined system of equations is obtained by merging the stiffness and force matrix from each domain. For test problems, the deformation and crack propagation in 2D elastic bodies subjected to quasi-static loads were analyzed. The numerical results clearly demonstrate the accuracy and efficiency of the proposed method for crack problems based on coupling the BEM and PD.

© 2021 Elsevier Ltd. All rights reserved.

1. Introduction

Crack analysis is still a major challenge within the framework of classical continuum mechanics. This is because partial differential equations (PDEs) are often applied in continuum mechanics, while for crack analysis, the spatial derivatives are not defined either at the crack tip or along the crack surfaces. This contradicts the assumption that the elastic body remains continuous as it deforms. Therefore, the basis of the continuum formulation breaks down whenever a crack appears in a body. To tackle this inherent limitation in computational models using the finite element (FEM), boundary element (BEM), or meshfree methods, many special techniques such as remeshing (Nishioka, 1997; Liu et al., 2017; Kou and Yang, 2019), and local enrichment functions (Belytschko and Black, 1999; Moës Nicolas and Dolbow, 1999), have been developed. Furthermore, additional crack growth criteria based on the fracture mechanics theory and using the concept of stress intensity factors are required to predict the crack propagation length and direction.

In 2000, a new theory called peridynamics (PD) was developed by Dr. Silling (Silling, 2000) and team (Silling et al., 2007), which establishes a connection between classical continuum mechanics and molecular dynamics, such as models based on non-local theory (Madenci and Oterkus, 2014). The PD theory uses spatial integral equations instead of PDEs, which is better suited for modeling bodies with discontinuities. For example, it can model the initiation and propagation of a crack automatically without resorting the additional criteria because material failure can be invoked in the material response model. Thus, PD theory has the potential to model complex crack propagation behaviors and has been widely studied in the analysis of crack propagation (Dias et al., 2017; Qiao et al., 2017; Han et al., 2019; Huang et al., 2015).

However, its non-local nature results in the PD having some inherent drawbacks, such as the surface effect, low computational efficiency, and difficulty in imposing boundary conditions. Hence, coupling techniques using PD theory with continuum mechanics have been proposed to take advantage of their salient features if the regions of potential failure can be identified prior to the analysis.

The FEM is very flexible and efficient for modeling problems without cracks; thus, most work focused on coupling FEM with PD. A straightforward method of coupling PD with FEM was sug-

* Corresponding authors.
E-mail addresses: yangy33@sustech.edu.cn (Y. Yang), liuyj3@sustech.edu.cn (Y. Liu).

https://doi.org/10.1016/j.ijsolstr.2021.02.002
0020-7683/© 2021 Elsevier Ltd. All rights reserved.

gested by Macek and Silling (2007), in which the PD interactions are represented by using traditional truss elements and an embedded element technique for the overlap region. Lall et al. (2010) also utilized this approach to study the shock and vibration reliability of electronics. Kilic and Madenci (Kilic and Madenci, 2009) introduced a direct coupling of FEM and PD theory using an overlap region. Both the PD and FE equations are satisfied in the overlap region. The displacement and velocity of overlap are determined using FE equations and the body force densities determined by the PD theory. Finally, these body force densities serve as external forces for finite elements in the overlap region. Liu and Hong (2012) adopted interface elements between the FEM and PD regions. A finite number of PD points are embedded inside the interface element to transfer information between the PD and FEM regions. The PD forces exerted on these embedded material points are distributed as nodal forces to the interface element based on two particular schemes. Lubineau et al. (2012) combined the local and nonlocal theories by introducing a transition (morphing) strategy. The definition of the morphing functions relies on the energy equivalence, and the transition region affects only the constitutive parameters. This technique reformulated it in state-based PD by Han et al. (2016). A simple coupling approach is submodeling, as demonstrated by Oterkus et al. (2012) and Agwai et al. (2012). It involves FEM for global analysis and PD theory for submodeling to perform failure prediction. Seleson et al. (2013) proposed a force-based blended model that combined the PD theory and classical elasticity using nonlocal weights composed of integrals of blending functions. They also generalized this approach to combine PD and higher-order gradient models of any order. Hybrid modeling methods of PD and FEM were discussed in the work of Zhang et al. (Zhang et al., 2016; Yu, 2017). A truss element was introduced to bridge the FE and PD subregions. An effective method to couple FEM meshes and PD grids for the solution of static equilibrium problems was developed by Galvanetto et al. (2016). Coupling was achieved by considering that PD bonds act only on PD nodes, whereas finite elements apply forces only on finite element nodes. Zaccariotto et al. (2017) coupled FEM meshes to PD grids adopting a non-uniform grid size and applied it to 1D, 2D, and 3D dynamic problems (Zaccariotto et al., 2017). A new variable horizon method for coupling PD to FEM proposed by Nikpayam and Kouchakzadeh (2019). In this method, PD converges to classical theory as the horizon continuously reduces across an intermediate element called "morakkab", and the creation of ghost forces was prevented by using a modified PD equation of motion based on the co-family concept.

Recently, coupling other numerical methods with PD to analyze crack propagation problems has been developed by numerous researchers. Liu et al. (2020) and Giannakeas et al. (2020) coupled the extended finite element method (XFEM) with PD to study the crack propagation and branching problems, wherein the XFEM can improve the computation efficiency, and the PD can predict the crack propagation orientation. Zheng et al. (2020) introduced a coupling approach of isogeometric analysis with a non-ordinary state-based PD. Zeng et al. (2020) combined PD and generalized interpolation material point (GIMP) method via volume modification to simulate transient responses, which can be applied to effectively simulate large deformations and multi-phase (solid–fluid-gas) interactions by mapping the remapping between material points and associated background nodes. Coupling of meshfree PD with the finite volume method for poroelastic problems was presented by Agrawal et al. (2020).

Compared with other numerical methods, the boundary element method (BEM) has some special advantages. Based on the fundamental solutions, BEM is a semi-analytical method that can achieve improved accuracy owing to the use of integrations. In addition, the BEM can simulate the models with only boundary elements, reducing the problem dimension by one. Thus, a method based on coupling the BEM with PD is a natural next step for solving crack problems. It can take advantage of their salient features and potentially achieve improved computational efficiencies. However, only one conference paper has provided an overview of the PD formulation with the extended boundary element method (XBEM) for dynamic fracture (Hattori and Trevelyan, 2017) to date, in which the fracture problem is initially solved with the XBEM to obtain the displacement field and the SIF. Then, a PD zone is defined around the crack tip and receives the displacements from the XBEM solution. If the crack propagation criteria are satisfied, the bounds between the particles in the PD zone break, generating a new crack path. The crack path was further discretized with the XBEM mesh. In a sense, it is not a fully coupled method. Therefore, a method with a full combination of BEM and PD needs to be developed and studied.

In this paper, a new method by coupling the BEM with PD to predict propagation of cracks in two-dimensional (2D) bodies under quasi-static load is presented. The proposed method has not been previously reported. Herein, the cracked domain is simulated using the bond-based PD theory. Instead of constructing the bond force equations, a stiffness equation is established using Taylor's series expansion for the stretch. The traditional BEM is used to model the non-cracked domain. Similar to the sharing node-based coupling approach, there is no overlapped zone in the proposed coupling model. The displacements are continuous at the interface points, and the transferred force values can be easily determined by directly computing the interactions between the PD material points and BEM boundary nodes. A combined system of equations is obtained by merging the stiffness and force matrices for each domain. The accuracy of the proposed coupling approach is verified using three examples of uncracked models under static loads. Examples of mode I, mix mode, and two edge cracks, are analyzed to investigate the efficiency of this newly presented coupling approach.

2. Formulations

2.1. Boundary integral equations

For a 2D linear elastic and homogeneous domain Ω with boundary Γ, the displacement field can be represented by the following boundary integral equation (BIE) without considering the body force (Liu, 2009):

$$\frac{1}{2}u_i(\mathbf{x}) = \int_\Gamma U_{ij}(\mathbf{x},\mathbf{y})t_j(\mathbf{y})d\Gamma - \int_\Gamma T_{ij}(\mathbf{x},\mathbf{y})u_j(\mathbf{y})d\Gamma \tag{1}$$

where u_i is the displacement, t_i is the traction, $U_{ij}(\boldsymbol{x},\boldsymbol{y})$ and $T_{ij}(\boldsymbol{x},\boldsymbol{y})$ are the fundamental solutions (kernel functions) for the displacement and traction fields due to a unit point force at the source point $\mathbf{x}$, respectively. For the 2D plane strain case, the two kernel functions are given by,

$$U_{ij}(\boldsymbol{x},\boldsymbol{y}) = \frac{-1}{8\pi G(1-\nu)}\left[(3-4\nu)\delta_{ij}\ln(r) - r_{,i}r_{,j}\right] \tag{2}$$

$$T_{ij}(\boldsymbol{x},\boldsymbol{y}) = \frac{-1}{4\pi(1-\nu)r}\left[(1-2\nu)(n_ir_j - n_jr_i) + ((1-2\nu)\delta_{ij} + 2r_ir_j)r_ln_l)\right] \tag{3}$$

where $G = E/2(1+\nu)$ and ν are the shear modulus and Poisson's ratio, respectively (For plane stress condition, Poisson's ratio ν in the preceding expressions is replaced with ν/(1 + ν)); r represents the distance from source point × to the field point $\mathbf{y}$, δ_{ij} is the

Kronecker symbol; and n_i is the direction cosine of the normal. A comma after a quantity represents spatial derivatives, and repeated indexes denote summation.

By discretizing the BIE with the quadratic boundary elements, we obtain the following BEM matrix equation:

$$\begin{bmatrix} \boldsymbol{T}_{11} & \boldsymbol{T}_{12} & \cdots & \boldsymbol{T}_{1N_B} \\ \boldsymbol{T}_{21} & \boldsymbol{T}_{22} & \cdots & \boldsymbol{T}_{2N_B} \\ \vdots & \vdots & \vdots & \vdots \\ \boldsymbol{T}_{N_B1} & \boldsymbol{T}_{N_B2} & \cdots & \boldsymbol{T}_{N_BN_B} \end{bmatrix} \begin{Bmatrix} \boldsymbol{u}_1 \\ \boldsymbol{u}_2 \\ \vdots \\ \boldsymbol{u}_{N_B} \end{Bmatrix} = \begin{bmatrix} \boldsymbol{U}_{11} & \boldsymbol{U}_{12} & \cdots & \boldsymbol{U}_{1N_B} \\ \boldsymbol{U}_{21} & \boldsymbol{U}_{22} & \cdots & \boldsymbol{U}_{2N_B} \\ \vdots & \vdots & \vdots & \vdots \\ \boldsymbol{U}_{N_B1} & \boldsymbol{U}_{N_B2} & \cdots & \boldsymbol{U}_{N_BN_B} \end{bmatrix} \begin{Bmatrix} \boldsymbol{t}_1 \\ \boldsymbol{t}_2 \\ \vdots \\ \boldsymbol{t}_{N_B} \end{Bmatrix} \tag{4}$$

where $\mathbf{u}_i$ and $\mathbf{t}_i$ are the displacement and traction vectors at node i on boundary Γ, respectively, (i = 1, 2, …, N_B, where N_B is the number of boundary nodes), and $\mathbf{T}_{ij}$ and $\mathbf{U}_{ij}$ are 2×2 submatrices by integrating the T and U kernels on elements, respectively.

The internal nodes of the BEM domain in Fig. 1 can be simultaneously calculated using Eq. (1). After substituting the boundary conditions, by switching the columns in the two matrices, Eq. (4) can be represented by grouping the boundary nodes and internal nodes as follows:

$$\begin{bmatrix} H_{BB} & 0 \\ H_{IB} & I \end{bmatrix} \begin{Bmatrix} x_B \\ u_I \end{Bmatrix} = \begin{bmatrix} G_{BB} \\ G_{IB} \end{bmatrix} \{y_B\} \tag{5}$$

where $\mathbf{H}_{BB}$, $\mathbf{G}_{BB}$ and $\mathbf{H}_{IB}$, $\mathbf{G}_{IB}$ are submatrices for the boundary and internal nodes, respectively, comprising the dimensions of $2N_B \times 2N_B$ and $2N_I \times 2N_B$ (B for boundary nodes and I for internal nodes); $\mathbf{x}_B$ is the vector of unknown boundary values, and $\mathbf{y}_B$ is the known right-hand-side vector. Retaining the known vector $\mathbf{y}_B$ on the right side of the equation, a matrix operation is applied to Eq. (5) which yields,

$$\begin{bmatrix} \bar{\boldsymbol{H}}_{BB} & \boldsymbol{0} \\ \bar{\boldsymbol{H}}_{IB} & \boldsymbol{I} \end{bmatrix} \begin{Bmatrix} \boldsymbol{x}_B \\ \boldsymbol{u}_I \end{Bmatrix} = \begin{Bmatrix} \boldsymbol{y}_B \\ \boldsymbol{0} \end{Bmatrix} \tag{6}$$

in which, $\bar{\boldsymbol{H}}_{BB} = \boldsymbol{G}_{BB}^{-1}\boldsymbol{H}_{BB}$ and $\bar{\boldsymbol{H}}_{IB} = \left(\boldsymbol{H}_{IB} - \boldsymbol{G}_{IB}\boldsymbol{G}_{BB}^{-1}\boldsymbol{H}_{BB}\right)$.

Then, a standard linear system of equations for the BEM is formed as follows:

$$\begin{bmatrix} \boldsymbol{K}_{B_{11}} & \boldsymbol{K}_{B_{12}} & \cdots & \boldsymbol{K}_{B_{1N}} \\ \boldsymbol{K}_{B_{21}} & \boldsymbol{K}_{B_{22}} & \cdots & \boldsymbol{K}_{B_{2N}} \\ \vdots & \vdots & \vdots & \vdots \\ \boldsymbol{K}_{B_{N1}} & \boldsymbol{K}_{B_{N2}} & \cdots & \boldsymbol{K}_{B_{NN}} \end{bmatrix} \begin{Bmatrix} \boldsymbol{x}_{B_1} \\ \boldsymbol{x}_{B_2} \\ \vdots \\ \boldsymbol{x}_{B_N} \end{Bmatrix} = \begin{Bmatrix} \boldsymbol{y}_{B_1} \\ \boldsymbol{y}_{B_2} \\ \vdots \\ \boldsymbol{y}_{B_N} \end{Bmatrix} \text{or} [\boldsymbol{K}_B]\{\boldsymbol{x}_B\} = \{\boldsymbol{y}_B\} \tag{7}$$

where $\mathbf{K}_B$ is the coefficient matrix of dimensions $2\ N \times 2\ N$ (where N is the number of all the nodes in the BEM domain including boundary and internal nodes).

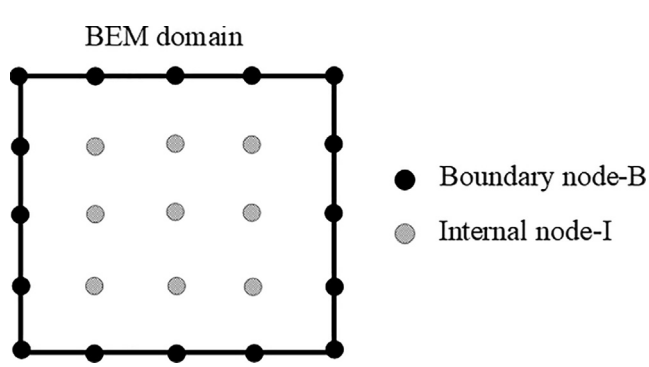

Fig. 1. Boundary and internal nodes of the BEM domain.

2.2. PD formulations

The bond-based PD theory was employed in this analysis. In this case, the Poisson's ratio is constrained to 1/3 in the plane stress condition for isotropic materials (Silling et al., 2007). The bond-based PD equation of motion is expressed as follows:

$$\rho_{(g)}\ddot{u}_{(g)}(t) = \int_{H_{(g)}} f\left[u_{(h)} - u_{(g)}, x_{(h)} - x_{(g)}, t\right] dH_{(g)} + b_{(g)}(t),\ \forall\ h \in H_{(g)} \tag{8}$$

where $H_{(g)}$ is the neighborhood of point g, which is usually taken to be a spherical region of radius δ centered at point g, as shown in Fig. 2; δ is the horizon representing the size of nonlocal interaction; $\mathbf{u}$ and ρ are the displacement vector and mass density, respectively, which are the same as in the continuum mechanics; $\mathbf{b}$ is the body force density vector, and $\mathbf{f}$ is the force density vector, referred to as the pairwise response function, which is defined as the force vector per unit volume that represents the force point h exerted on point g. When $\delta \to 0$, the peridynamic equation of motion in Eq. (8) is reduced to the classical equation of motion (Silling and Lehoucq, 2010).

For a micro-elastic material, the force function can be expressed as

$$\boldsymbol{f}(\boldsymbol{\eta}, \xi) = \frac{\partial w(\boldsymbol{\eta}, \xi)}{\partial \boldsymbol{\eta}} = \frac{\boldsymbol{\eta} + \xi}{|\boldsymbol{\eta} + \xi|} c(\xi, \delta) s,\ \forall \boldsymbol{\eta}, \xi \tag{9}$$

where $w(\boldsymbol{\eta}, \xi) = \frac{c(\xi,\delta)s^2|\xi|}{2}$ is the micro-elastic potential, $\xi = \boldsymbol{x}_{(h)} - \boldsymbol{x}_{(g)}$ is the initial relative position, $\boldsymbol{\eta} = \boldsymbol{u}_{(h)} - \boldsymbol{u}_{(g)}$ is the current relative displacement, and s represents the stretch of a bond, that is related to the strain vector in continuum mechanics and is expressed as,

$$s = \frac{|\boldsymbol{\eta} + \xi| - |\xi|}{|\xi|} \tag{10}$$

Apply Taylor's series expansion for scalar function with multiple variables

$$f(\boldsymbol{x}) = f(\boldsymbol{x}_0) + \frac{\partial f(\boldsymbol{x}_0)}{\partial \boldsymbol{x}} \cdot (\boldsymbol{x} - \boldsymbol{x}_0),$$

and let $\boldsymbol{x} = \xi$, $\boldsymbol{x}_0 = \xi + \boldsymbol{\eta}$, $f(\boldsymbol{x}) = |\xi|$, and $f(\boldsymbol{x}_0) = |\xi + \boldsymbol{\eta}|$. Then s can be written as:

$$s = \left[\frac{\partial|\xi|}{\partial \xi}\bigg|_{\xi=\xi+\boldsymbol{\eta}}\right] \cdot \frac{\boldsymbol{\eta}}{|\xi|} = \frac{\boldsymbol{\eta} + \xi}{|\boldsymbol{\eta} + \xi|} \cdot \frac{\boldsymbol{\eta}}{|\xi|} \tag{11}$$

Substituting of Eqs. (11) into (9), the pairwise force can be written as,

$$\boldsymbol{f}(\boldsymbol{\eta}, \xi) = \frac{c(\xi, \delta)}{|\xi|}\boldsymbol{\eta} = \frac{c(\xi, \delta)}{|\xi|}\left(\boldsymbol{u}_{(h)} - \boldsymbol{u}_{(g)}\right) \tag{12}$$

where $c(\xi, \delta) = c(0, \delta)g(\xi, \delta)$ is the micro-modulus function that contains all material-specific information. The modified micro-modulus function expression proposed by Huang et al. (2015) is used in this analysis, which is

$$g(\xi, \delta) = \begin{cases} \left(1 - \left(\frac{|\xi|}{\delta}\right)^2\right)^2, & |\xi| \leqslant \delta \\ 0, & |\xi| > \delta \end{cases} \text{and}\ c(0, \delta) = \begin{cases} \frac{72E}{\pi\delta^4}, & 3D \\ \frac{315E}{8\pi\delta^3}, & \text{plane stress} \\ \frac{210E}{5\pi\delta^3}, & \text{plane strain} \end{cases} \tag{13}$$

where E is the macroscopic Young's modulus. This expression not only satisfies the non-local nature of the PD theory precisely, but also reflects the weakening of the long-range force intensity when the distance between two particles increases. In order to guarantee the same material are considered in BEM and PD domain, the material properties should be identical. To include

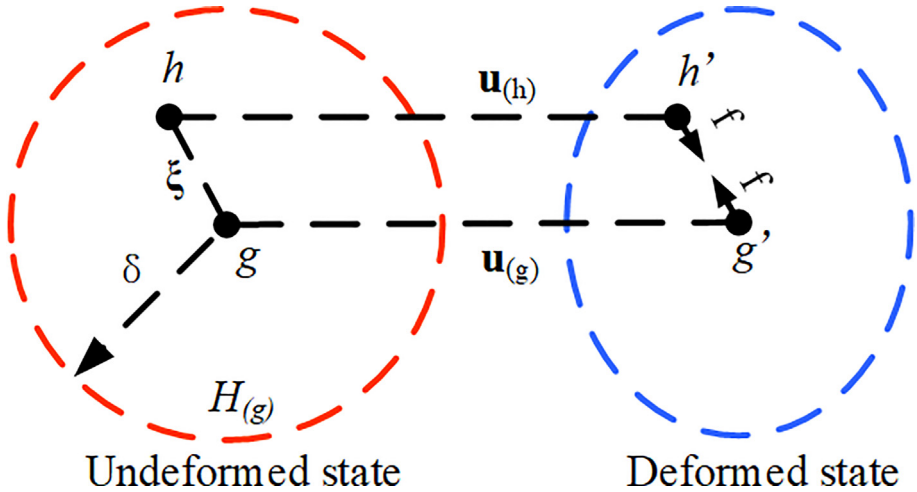

Fig. 2. Bond-based PD theory discerption.

damage initiation in the material response, the force density vector can be modified through a history-dependent scalar valued function μ as,

$$\mu(\xi,t)=\begin{cases}1, & \text{if } s(\xi,t')<s_c \text{ for all } 0\leqslant t'\leqslant t\\ 0, & \text{otherwise}\end{cases} \tag{14}$$

When the stretch s between these material points exceeds its critical stretch s_c, failure occurs; thus, μ is zero, rendering the associated portion of the force density vector to be zero. Critical stretch s_c is related to the fracture energy G_0, which denotes the energy per unit crack length in 2D, required for a complete separation of the body into two parts. For plane stress, s_c can be derived as (Huang et al., 2015);

$$s_c=\sqrt{\frac{1024\pi G_0}{7(120\pi\text{ - }133)E\delta}} \tag{15}$$

Local damage at a point is defined as the weighted ratio of the number of eliminated interactions to the total number of initial interactions of a material point with its family members. The local damage at a point can be quantified as (Silling et al., 2007):

$$\varphi(g,t)=1-\frac{\int_{H_{(g)}}\mu(\xi,t)dV_{(h)}}{\int_{H_{(g)}}dV_{(h)}} \tag{16}$$

The numerical approximation of the PD equation starts with the subdivision of the structure into nodes, and each node is associated with a certain volume $V_{(h)}$, and the union of all volumes covers the entire body volume. Therefore, for each time step, the discretized form of Eq. (8) is:

$$\rho\ddot{\mathbf{u}}^n_{(g)}=\sum_h \boldsymbol{f}\left[\boldsymbol{u}^n_{(h)}-\boldsymbol{u}^n_{(g)},\mathbf{x}^n_{(h)}-\mathbf{x}^n_{(g)}\right]\upsilon^n_{(h)}V^n_{(h)}\mu^n(\xi)+\boldsymbol{b}^n_{(g)},\ \forall\ h\in H_{(g)} \tag{17}$$

For the static problem, the time dependence is removed from Eq. (17), and the term on the left-hand side is set to zero because the problem can be studied as a sequence of static analyses with incremental external loads or displacements. The equation solved in the present study is therefore,

$$\mathbf{0}=\sum_h \boldsymbol{f}\left[\boldsymbol{u}^n_{(h)}-\boldsymbol{u}^n_{(g)},\boldsymbol{x}^n_{(h)}-\boldsymbol{x}^n_{(g)}\right]\upsilon^n_{(h)}V^n_{(h)}\mu^n(\xi)+\boldsymbol{b}^n_{(g)},\ \forall\ h\in H_{(g)} \tag{18}$$

Substituting the pairwise force defined in Eq. (12) yields,

$$\sum_h \frac{c}{|\xi|_{(h)(g)}}\left(\boldsymbol{u}^n_{(g)}-\boldsymbol{u}^n_{(h)}\right)\upsilon^n_{(h)}V^n_{(h)}\mu^n(\xi)=\boldsymbol{b}^n_{(g)},\ \forall\ h\in H_{(g)} \tag{19}$$

where $V_{(h)}$ and $\upsilon_{(h)}$ are the volume and volume reduction factor for material point h, respectively. When the volume $V_{(h)}$ of the family node h falls completely within the horizon of the central node g, $\upsilon_{(h)}$ is equal to 1, and when $\delta-\Delta x/2<|\xi|_{(h)(g)}<\delta$, $\upsilon_{(h)}=\left(\delta+\Delta x/2-|\xi|_{(h)(g)}\right)/\Delta x$, where Δx is the spacing of material points.

By introducing the stiffness matrix with coefficient $K_{(g)(h)}$, we can rewrite Eq. (19) for each step as,

$$\sum_h \boldsymbol{K}_{(g)(h)}\left(\boldsymbol{u}_{(g)}-\boldsymbol{u}_{(h)}\right)=\boldsymbol{b}_{(g)},\ \forall\ h\in H_{(g)},$$

where

$$\boldsymbol{K}_{(g)(h)}=\frac{c}{|\xi|_{(g)(h)}}\upsilon_{(h)}V_{(h)}\mu(\xi)\begin{bmatrix}l^2 & lm & -l^2 & -lm\\ lm & m^2 & -lm & -m^2\end{bmatrix} \tag{20}$$

$l_{(g)(h)}=\cos\theta_1=\frac{x_{(h)}-x_{(g)}}{|\xi_{(h)(g)}|}$, and $m_{(g)(h)}=\cos\theta_2=\frac{y_{(h)}-y_{(g)}}{|\xi_{(h)(g)}|}$ are the coordinate transformation parameters (Fig. 3). $x_{(h)}$, $x_{(g)}$ and $y_{(h)}$, $y_{(g)}$ are x coordinates and y coordinates for points h and g, respectively.

Then, the stiffness matrix equation for material point g can be written as follows:

$$\begin{bmatrix}\frac{c_{(g)(h_1)}\upsilon_{(h_1)}V_{(h_1)}l^2_{(g)(h_1)}}{|\xi|_{(g)(h_1)}}+\cdots+\frac{c_{(g)(h_n)}\upsilon_{(h_n)}V_{(h_n)}l^2_{(g)(h_n)}}{|\xi|_{(g)(h_n)}} & \frac{c_{(g)(h_1)}\upsilon_{(h_1)}V_{(h_1)}l_{(g)(h_1)}m_{(g)(h_1)}}{|\xi|_{(g)(h_1)}}+\cdots+\frac{c_{(g)(h_1)}\upsilon_{(h_1)}V_{(h_1)}l_{(g)(h_1)}m_{(g)(h_1)}}{|\xi|_{(g)(h_1)}}\\ \frac{c_{(g)(h_1)}\upsilon_{(h_1)}V_{(h_1)}l_{(g)(h_1)}m_{(g)(h_1)}}{|\xi|_{(g)(h_1)}}+\cdots+\frac{c_{(g)(h_1)}\upsilon_{(h_1)}V_{(h_1)}l_{(g)(h_1)}m_{(g)(h_1)}}{|\xi|_{(g)(h_1)}} & \frac{c_{(g)(h_1)}\upsilon_{(h_1)}V_{(h_1)}m^2_{(g)(h_1)}}{|\xi|_{(g)(h_1)}}+\cdots+\frac{c_{(g)(h_n)}\upsilon_{(h_n)}V_{(h_n)}m^2_{(g)(h_n)}}{|\xi|_{(g)(h_n)}}\\ -\frac{c_{(g)(h_1)}\upsilon_{(h_1)}V_{(h_1)}}{|\xi|_{(g)(h_1)}}l^2_{(g)(h_1)} & -\frac{c_{(g)(h_1)}\upsilon_{(h_1)}V_{(h_2)}}{|\xi|_{(g)(h_1)}}l_{(g)(h_1)}m_{(g)(h_1)}\\ -\frac{c_{(g)(h_1)}\upsilon_{(h_1)}V_{(h_1)}}{|\xi|_{(g)(h_1)}}l_{(g)(h_1)}m_{(g)(h_1)} & -\frac{c_{(g)(h_1)}\upsilon_{(h_1)}V_{(h_1)}}{|\xi|_{(g)(h_1)}}m^2_{(g)(h_1)}\\ \vdots & \vdots\\ -\frac{c_{(g)(h_n)}\upsilon_{(h_n)}V_{(h_n)}}{|\xi|_{(g)(h_n)}}l^2_{(g)(h_n)} & -\frac{c_{(g)(h_n)}\upsilon_{(h_n)}V_{(h_n)}}{|\xi|_{(g)(h_n)}}l_{(g)(h_n)}m_{(g)(h_n)}\\ -\frac{c_{(g)(h_n)}\upsilon_{(h_n)}V_{(h_n)}}{|\xi|_{(g)(h_n)}}l_{(g)(h_n)}m_{(g)(h_n)} & -\frac{c_{(g)(h_n)}\upsilon_{(h_n)}V_{(h_n)}}{|\xi|_{(g)(h_n)}}m^2_{(g)(h_n)}\end{bmatrix}^T\begin{Bmatrix}u_{(g)}\\ v_{(g)}\\ u_{(h_1)}\\ v_{(h_1)}\\ \vdots\\ u_{(h_n)}\\ u_{(h_n)}\end{Bmatrix}=\begin{Bmatrix}b_{(g)_x}\\ b_{(g)_y}\end{Bmatrix} \tag{21}$$

The discretized form of Eq. (19) can also be written in a standard linear system of equations as follows:

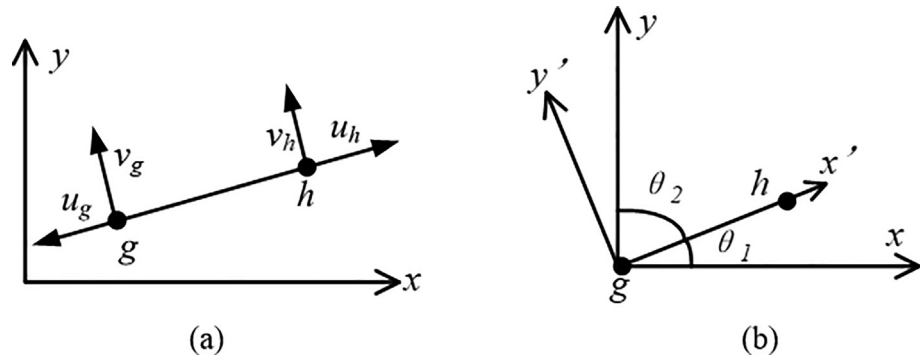

Fig. 3. The coordinate transformation.

$$\begin{bmatrix} \boldsymbol{K}_{P_{11}} & \boldsymbol{K}_{P_{12}} & \cdots & \boldsymbol{K}_{P_{1M}} \\ \boldsymbol{K}_{P_{21}} & \boldsymbol{K}_{P_{22}} & \cdots & \boldsymbol{K}_{P_{2M}} \\ \vdots & \vdots & \vdots & \vdots \\ \boldsymbol{K}_{P_{M1}} & \boldsymbol{K}_{P_{M2}} & \cdots & \boldsymbol{K}_{P_{MM}} \end{bmatrix} \begin{Bmatrix} \boldsymbol{u}_{P_1} \\ \boldsymbol{u}_{P_2} \\ \vdots \\ \boldsymbol{u}_{P_M} \end{Bmatrix} = \begin{Bmatrix} \boldsymbol{b}_{P_1} \\ \boldsymbol{b}_{P_2} \\ \vdots \\ \boldsymbol{b}_{P_M} \end{Bmatrix} \text{or } [\boldsymbol{K}_P]\{\boldsymbol{u}_P\} = \{\boldsymbol{b}_P\} \tag{22}$$

where $\mathbf{K}_P$ is the coefficient matrix of dimensions $2M \times 2M$ (M is the total number of material points), $\mathbf{u}_P$ is the displacement vector, and $\mathbf{b}_P$ is the body force vector.

2.3. Formulation for coupling the BEM and PD

A model using shared nodes is established to combine the BEM and PD equations, as depicted in Fig. 4. Based on the scale and location of cracks, the entire structure is divided into several domains. The domain without cracks is discretized using the boundary elements and is referred to as the BEM domain. The domain in which cracks exist and propagate is simulated by material points and is known as the PD domain. For the sake of description, three point types are introduced: The nodes belonging only to the BEM domain are denoted as "B," which implies BEM itself; while the material points within the PD domain are simplified as "P," the interface points in the BEM domain are BEM nodes denoted as "C_B," and they are also the material points in the PD domain, therefore, also denoted as "C_P."

First, the stiffness matrix for each domain was constructed. Consider a two-domain structure as an example. In the BEM domain, Eq. (7) is rewritten for "B" and "C_B" nodes as follows:

$$\begin{bmatrix} \boldsymbol{K}^n_{BB} & \boldsymbol{K}^n_{BC_B} \\ \boldsymbol{K}^n_{C_BB} & \boldsymbol{K}^n_{C_BC_B} \end{bmatrix} \begin{Bmatrix} \boldsymbol{x}^n_B \\ \boldsymbol{u}^n_{C_B} \end{Bmatrix} = \begin{Bmatrix} \boldsymbol{y}^n_B \\ \boldsymbol{t}^n_{C_B} \end{Bmatrix} \tag{23}$$

In the PD domain, the stiffness matrix in Eq. (22) for "C_P" and "P" material points is written as,

$$\begin{bmatrix} \mathbf{K}^n_{C_PC_P} & \boldsymbol{K}^n_{C_PP} \\ \boldsymbol{K}^n_{PC_P} & \boldsymbol{K}^n_{PP} \end{bmatrix} \begin{Bmatrix} \boldsymbol{u}^n_{C_P} \\ \boldsymbol{u}^n_P \end{Bmatrix} = \begin{Bmatrix} \boldsymbol{b}^n_{C_P} \\ \boldsymbol{b}^n_P \end{Bmatrix} \tag{24}$$

where $\boldsymbol{K}^n_{BB}$ and $\boldsymbol{K}^n_{PP}$ represent the *nth-step* stiffness matrix of the boundary nodes and material points, which belong to the BEM and PD regions only, respectively. $\boldsymbol{K}^n_{C_BC_B}$ and $\boldsymbol{K}^n_{C_PC_P}$ represent the *nth*-step stiffness matrix of the nodes that are on the interface for the BEM simulation and PD simulation, respectively.

The displacement continuity at the interface nodes is expressed as,

$$\left\{\boldsymbol{u}^n_{C_B}\right\} = \left\{\boldsymbol{u}^n_{C_P}\right\} = \{\boldsymbol{u}^n_C\} \tag{25}$$

On the other hand, the force acting on the interface nodes from the BEM domain is opposite to that from the PD domain obeying Newton's third law. However, the traction force computed in the BEM domain is different from the body force calculated in the PD domain. Thus, an equivalent traction for the body force should be first performed by using the following equations:

$$\begin{matrix} t_i = \sigma_{ij}n_j \\ -b_i = \sigma_{ij,j} \end{matrix} \rightarrow t_i = \int \sigma_{ij,j}dx = -\int b_i dx \rightarrow \left\{\boldsymbol{t}^n_{C_B}\right\} = -\left\{\boldsymbol{b}^n_{C_P} \cdot \Delta x\right\} \tag{26}$$

where Δx is the spacing of the material points.

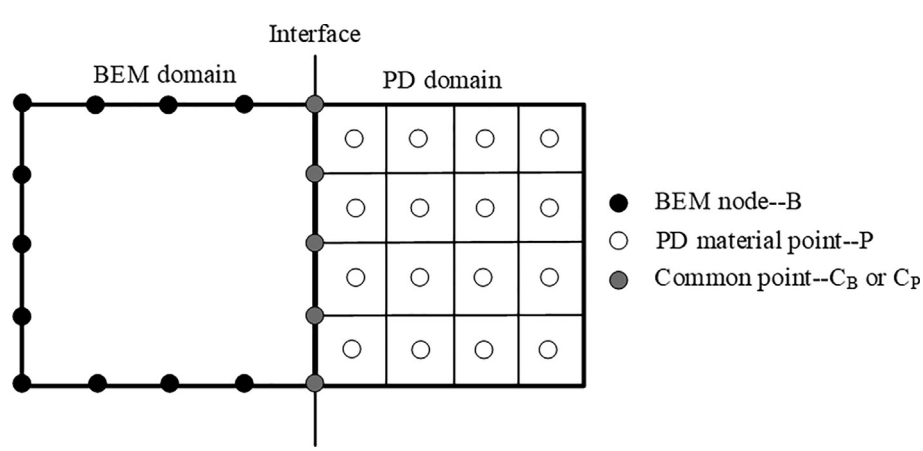

Fig. 4. The BEM and PD coupling model of two domains.

Before coupling the two systems of equations, one important consideration is that the stiffness matrices of different domains have different forms. For the BEM domain, the stiffness matrix is full and nonsymmetrical; however, the stiffness matrix of the PD domain is banded and symmetrical. Although, the forms of the stiffness matrix for the PD domain are much different from that of the BEM domain, these two systems can couple directly and obtain a robust system of equations. Finally, based on Eqs. (25) and (26) for the interface conditions, the general stiffness matrix for the entire structure can be obtained by merging Eqs. (23) and (24).

$$\begin{bmatrix} \boldsymbol{K}^n_{BB} & \boldsymbol{K}^n_{BC_B} & \boldsymbol{0} \\ \boldsymbol{K}^n_{C_BB} & \boldsymbol{K}^n_{C_BC_B} + \left(\boldsymbol{K}^n_{C_PC_P}\cdot\Delta x\right) & \left(\boldsymbol{K}^n_{C_PP}\cdot\Delta x\right) \\ \boldsymbol{0} & \boldsymbol{K}^n_{PC_P} & \boldsymbol{K}^n_{PP} \end{bmatrix} \begin{Bmatrix} \boldsymbol{x}^n_B \\ \boldsymbol{u}^n_C \\ \boldsymbol{u}^n_P \end{Bmatrix} = \begin{Bmatrix} \boldsymbol{y}^n_B \\ \boldsymbol{0} \\ \boldsymbol{b}^n_P \end{Bmatrix} \tag{27}$$

The displacement of each boundary node and material point can be obtained by directly solving Eq. (27). The same procedures are applied to treat multi-domain structures. For example, the stiffness matrix for two BEM domains and one PD domain, as shown in Fig. 5, can be written as in Eq. (28).

$$\begin{bmatrix} \boldsymbol{K}^n_{B_IB_I} & \boldsymbol{K}^n_{B_IC_{B_I}} & \boldsymbol{0} & \boldsymbol{0} & \boldsymbol{0} \\ \boldsymbol{K}^n_{C_{B_I}B_I} & \boldsymbol{K}^n_{C_{B_I}C_{B_I}} + \left(\boldsymbol{K}^n_{C_{P_I}C_{P_I}}\cdot\Delta x\right) & \left(\boldsymbol{K}^n_{C_{P_I}P}\cdot\Delta x\right) & \left(\boldsymbol{K}^n_{C_{P_I}C_{P_{II}}}\cdot\Delta x\right) & \boldsymbol{0} \\ \boldsymbol{0} & \boldsymbol{K}^n_{PC_{P_I}} & \boldsymbol{K}^n_{PP} & \boldsymbol{K}^n_{PC_{P_{II}}} & \boldsymbol{0} \\ \boldsymbol{0} & \left(\boldsymbol{K}^n_{C_{P_{II}}C_{P_I}}\cdot\Delta x\right) & \left(\boldsymbol{K}^n_{C_{P_{II}}P}\cdot\Delta x\right) & \left(\boldsymbol{K}^n_{C_{P_{II}}C_{P_{II}}}\cdot\Delta x\right) + \boldsymbol{K}^n_{C_{B_{II}}C_{B_{II}}} & \boldsymbol{K}^n_{C_{B_{II}}B_{II}} \\ \boldsymbol{0} & \boldsymbol{0} & \boldsymbol{0} & \boldsymbol{K}^n_{B_{II}C_{B_{II}}} & \boldsymbol{K}^n_{B_{II}B_{II}} \end{bmatrix} \begin{Bmatrix} \boldsymbol{x}^n_{B_I} \\ \boldsymbol{u}^n_{C_I} \\ \boldsymbol{u}^n_P \\ \boldsymbol{u}^n_{C_{II}} \\ \boldsymbol{x}^n_{B_{II}} \end{Bmatrix} = \begin{Bmatrix} \boldsymbol{y}^n_{B_I} \\ \boldsymbol{0} \\ \boldsymbol{b}^n_P \\ \boldsymbol{0} \\ \boldsymbol{y}^n_{B_{II}} \end{Bmatrix} \tag{28}$$

2.4. Crack propagation calculations

For each step, the static forces or displacements (right side of Eqs. (27) and (28)) are updated. After obtaining the displacements of the material points, the stretch between two material points $s_{(g)(h)}$ is compared with the critical stretch s_c. If $s_{(g)(h)} < s_c$, the computational process continues until $s_{(g)(h)} > s_c$, that is, the bond between two material points breaks. The history-dependent scalar is set to zero, and the stiffness matrix [**K**] in Eq. (24) is updated, and then the computational steps continue. The detailed calculation procedure is illustrated in the flowchart shown in Fig. 6. Damage D is the local damage at the material point can be calculated by Eq. (16) Fig. 7.

3. Verifications

To verify the accuracy and efficiency of the developed approach, three verification examples are studied, and the numerical results are presented. The geometry of the considered examples has a length of 1.0 m and height of 0.2 m. For the material property, the Young's modulus is 100 GPa and the Poisson's ratio is 1/3. Throughout the analysis, a plane stress condition is assumed, and quadratic boundary elements are applied. The horizon in the PD model is $\delta = 4\Delta x$.

Example 1:. *Deformation of a 2D elastic domain*

A 2D elastic domain with left end fixed and right end subjected to a tensile load P = 1050 KN/m is first considered. The structure is divided into two regions of equal length, as shown in Fig. 6. Five different discretization cases are considered, and the results are discussed. The analytical solution for the elongation of this 2D domain is given by,

$$\Delta = \frac{PL}{EA} \tag{29}$$

where L and A are the length and cross-sectional area of the example, respectively. The external tensile distribution loads can be applied as body loads through the last right layer material points (Silling et al., 2007). The magnitude of body force applied to collocation points inside this region can be obtained by using Eq. (30). In which, H is the vertical length of the domain, and N_f is number of the nodes which subjected on the external force.

$$b_i = \frac{PH}{N_f} \tag{30}$$

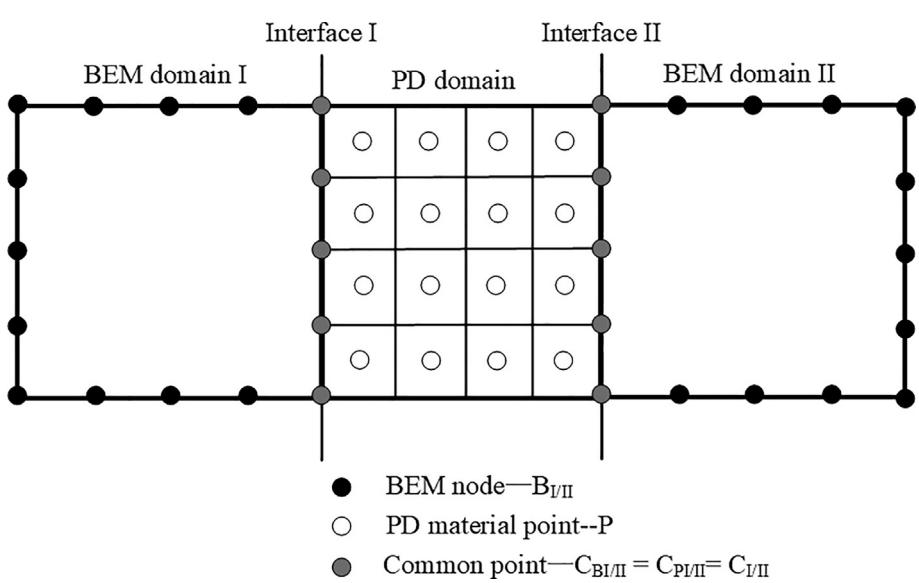

Fig. 5. The BEM and PD coupled model with three domains.

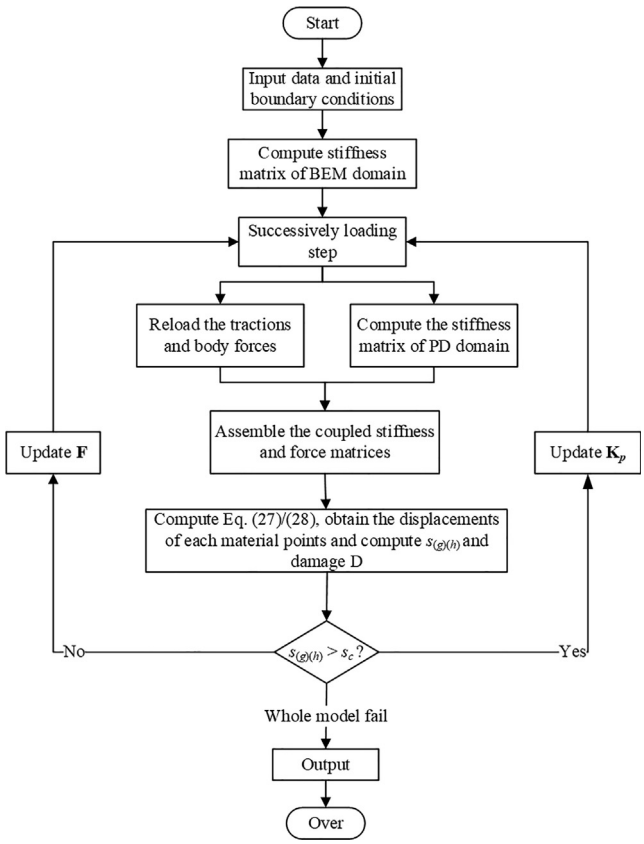

Fig. 6. Flowchart of the computational procedure.

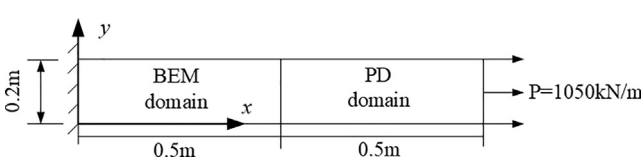

Fig. 7. A 2D elastic domain under tension.

Table 1
Five different discretization cases.

Cases	Numbers of BE and MP
Case 1	28 BE and 45 MP
Case 2	28 BE and 1000 MP
Case 3	60 BE and 1000 MP
Case 4	140 BE and 1000 MP
Case 5	100 BE and 4000 MP

To investigate the effect of the node distance and material point spacing on the computed results based on the coupling model, five different discretization cases are considered and listed in Table 1. Because the BEM and PD domains share the same nodes on the interface, the uniform (Cases 1 and 3–5) and nonuniform (Case 2) material point spacings are discussed separately. For the uniform material point spacing case, the node distances on the vertical edges in the BEM domain are the same as the material point spacing in the PD domain; In contrast, nonuniform case is that the nodes distance on the interfaces are not identical with the material points spacing Δx. In Fig. 8, four uniform discretization models are

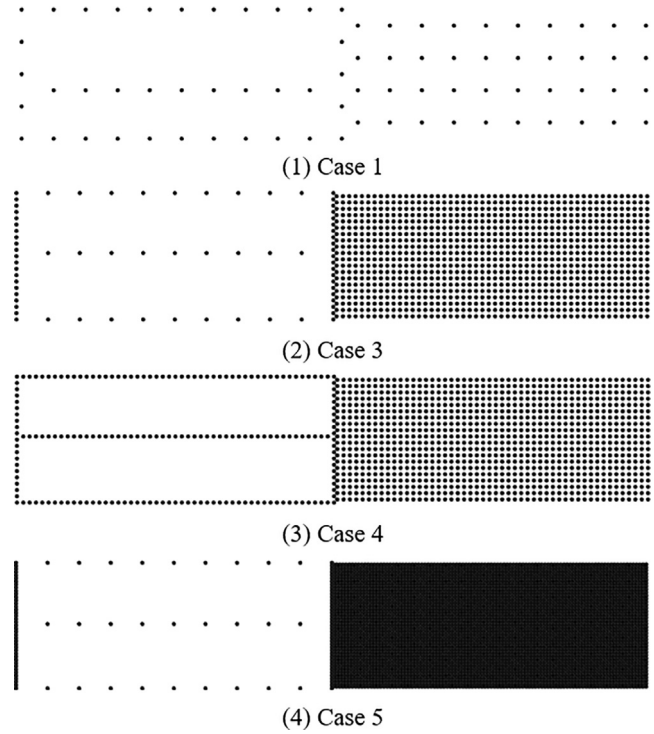

Fig. 8. Four discretization cases of the BEM and PD domains.

plotted. The node distances on the vertical edges and material point spacing vary from 0.05 m to 0.005 m. Uniform and nonuniform node distances in the BEM domain are also discussed. Cases 1 and 4 have uniform node distances. However, for Cases 3 and 5, the node distances on the vertical edges are not the same as those on the longitudinal edges, which are denoted as nonuniform node distance cases. The internal nodes in BEM domain are used to compute the central line results to compare with the analytical solutions. The computed results of the displacement field obtained using the present coupling approach are compared with the analytical solutions and are shown in Fig. 9 and Table 2. The contour plots of the displacement components u_1 and u_2 are also shown in Fig. 10.

From Fig. 9 and Table 2, it can be observed that the present coupling approach can yield accurate results even when only a few boundary elements (BE) and material points (MP) are used. The results are in good agreement with the analytical solutions. In Table 2, the interface and result errors are defined by the differences between the present results and the analytical solutions at the interface and the right end mid-points, respectively. Increasing the number of BE and MP nodes improves the interface connection and thus, the computed results. The consistency of the node distances along the longitudinal and vertical edges in the BEM domain is found to have less effect on the coupling model results. The horizon δ is also investigated in detail. In general, the computed results were found to be stable when $\delta \geq 3\Delta x$ (Silling et al., 2007).

One nonuniform material point spacing along the interface was also considered in the analysis. The distance of the BE nodes on the interface is 0.05 m, and the PD material point spacing is 0.01 m. The discretization and results of this model are plotted in Fig. 11. It can be seen that the nonuniform spacing negatively affects the results. The error between the BEM domain results and the analytical solution is noticeable, as shown on the left part of Fig. 11. The continuity of the displacement field is also poor at the interface, as depicted in (b) and (c) of Fig. 11.

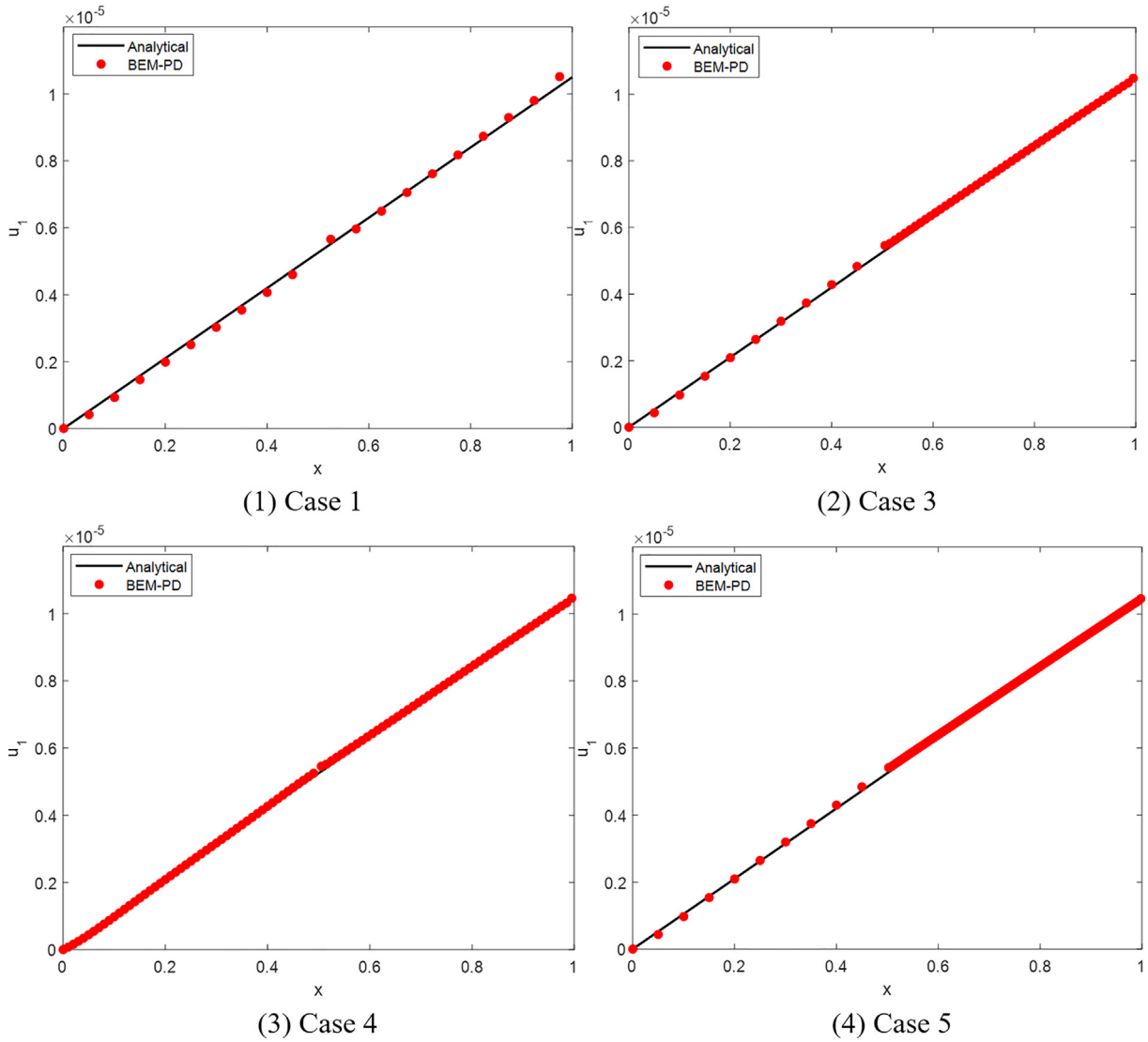

Fig. 9. Computed results of u_1 along the x axis compared with the analytical solution.

Table 2
Computing time and solution error for Example 1.

Cases	Numbers of BE and MP	Time (s)	Interface Error (%)	Results error (%)
Case 3	60 BE and 1000 MP	1.08	2.90	0.31
Case 4	140 BE and 1000 MP	9.34	2.89	0.12
Case 5	100 BE and 4000 MP	10.02	2.65	0.13

Example 2:. *A 2D elastic domain under a shear force*

A 2D elastic domain of the same geometry as in the previous example is studied next, where a concentrated force P = 100 kN is applied at the upper right corner (Fig. 12). The analytical solution of the deflection of this example at the free end is given by

$$y = -\frac{Px^2}{6EI}(3L - x), \textit{with the maximum deflection given } y_{\max} = -\frac{PL^3}{3EI} \tag{31}$$

The BEM and PD coupling approach results are compared with those of the analytical solution, as shown in Fig. 13 and Table 3. The present results match very well with those of the analytical solution except for Case 2, in which the material spacing is not uniform for the interface nodes and the continuity is not consistent. This can be seen in the u_1 contour plot of Case 2 in Fig. 14 with a slightly noted change near the interface. The results of the coupled FEM and PD method (Yu, 2017) are also listed in Table 3. In Ref. (Yu, 2017), compared with the results of the BEM and PD coupling approach, many more finite elements and material points are employed, but with less efficiency and accuracy in the results.

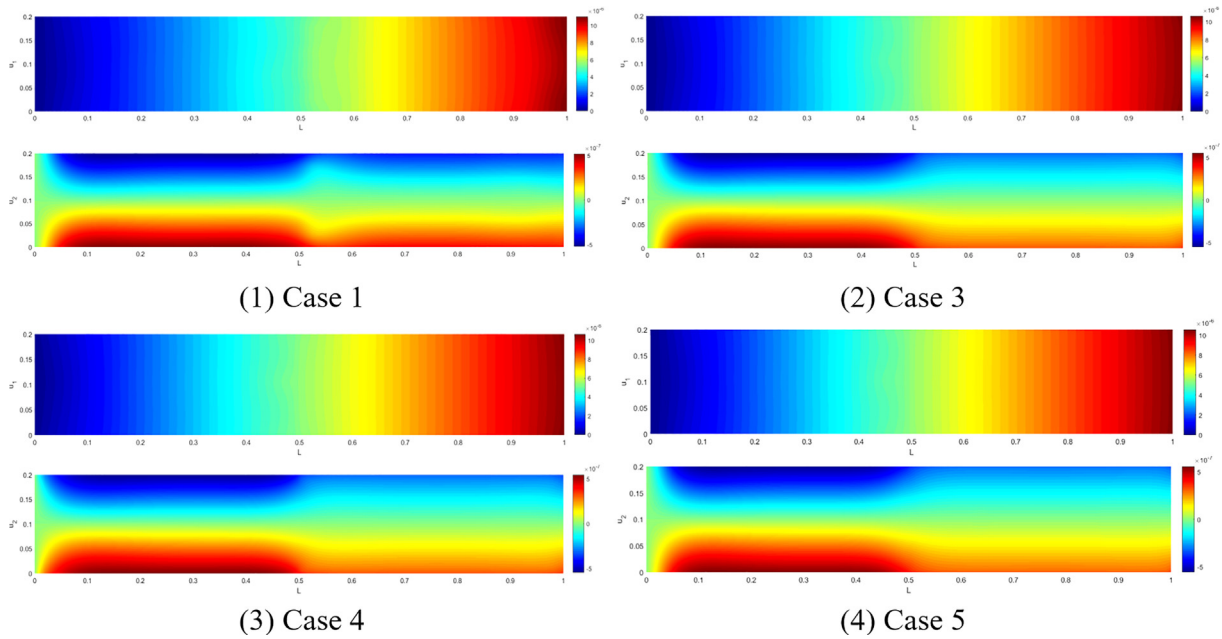

Fig. 10. Contour plots of the displacement components u_1 and u_2.

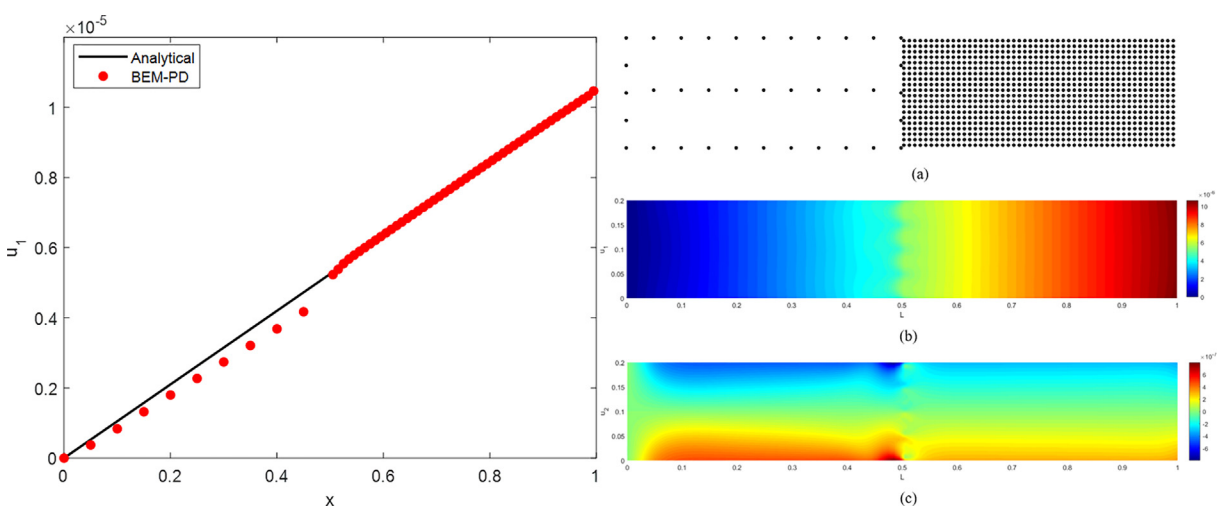

Fig. 11. Results of Case 2.

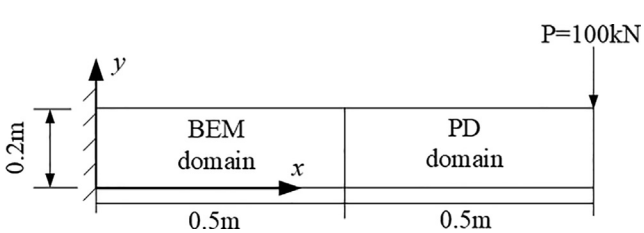

Fig. 12. A 2D elastic domain under a shear force.

The uniform material point spacing is more accurate than that with a nonuniform spacing. Thus, the uniform material point spacing in discretization will be used in all subsequent studies.

Example 3:. *Stretching of 2D elastic domain*

The elastic tensile 2D domain studied in Example 1 is subjected to two opposite displacement loads of 1 m at the left and right ends, as shown in Fig. 15 and discussed in this section. The entire domain is divided into three regions, the center part is the PD

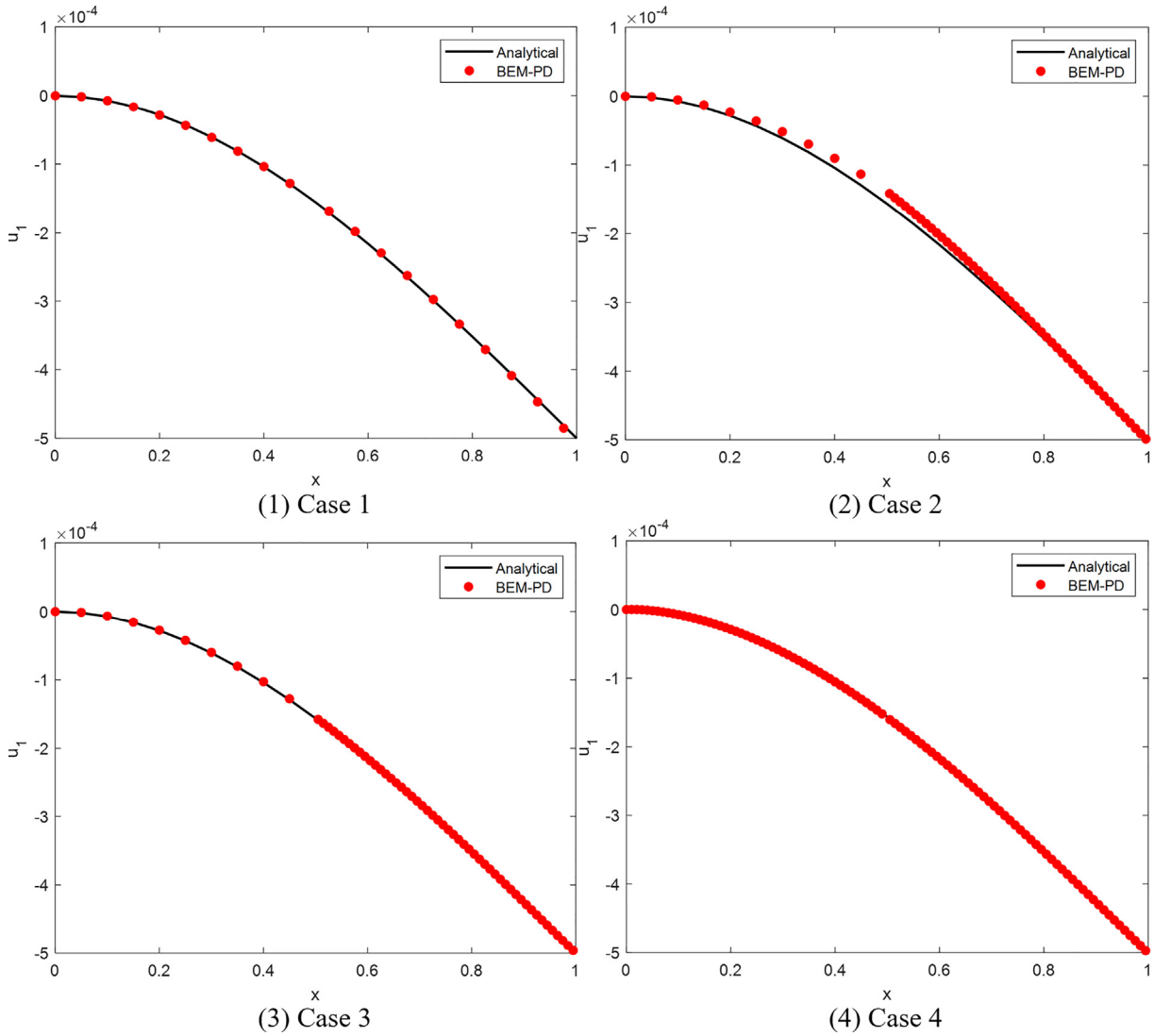

Fig. 13. Deflection of the beam compared with the analytical solution.

Table 3
Computing time and solution error for Example 2.

	Numbers of BE and MP	Time (s)	Interface error (%)	Results error (%)
Case 1	28 BE and 40 MP	0.14	5.99	0.82
Case 2	28 BE and 1000 MP	0.41	11.11	0.51
Case 3	60 BE and 1000 MP	1.05	0.86	0.05
Case 4	140 BE and 1000 MP	9.55	0.48	0.12
Yu (2017)	2500 FE and 40,000 MP	36	–	1.08

domain, and the sides are the BEM domains. Three uniform material point spacings, Δx = 0.05, 0.01, and 0.005 m, are investigated in detail. The discretization models are shown in Fig. 16 and Table 4.

Fig. 17 and Table 5 show the computed results and a comparison with the analytical solution and the computing times. It can be observed that fewer BE and MP nodes can yield satisfactory results, with the largest error near the interface. Increasing the BE and MP numbers can improve the interface continuity, as shown in Fig. 18, where the contour plotting of u_1 and u_2 of the problems are presented.

4. Applications in modeling crack propagation

Three examples of predicting the propagation of cracks in 2D elastic bodies have been presented in this section to demonstrate the effectiveness and efficiency of the developed BEM and PD cou-

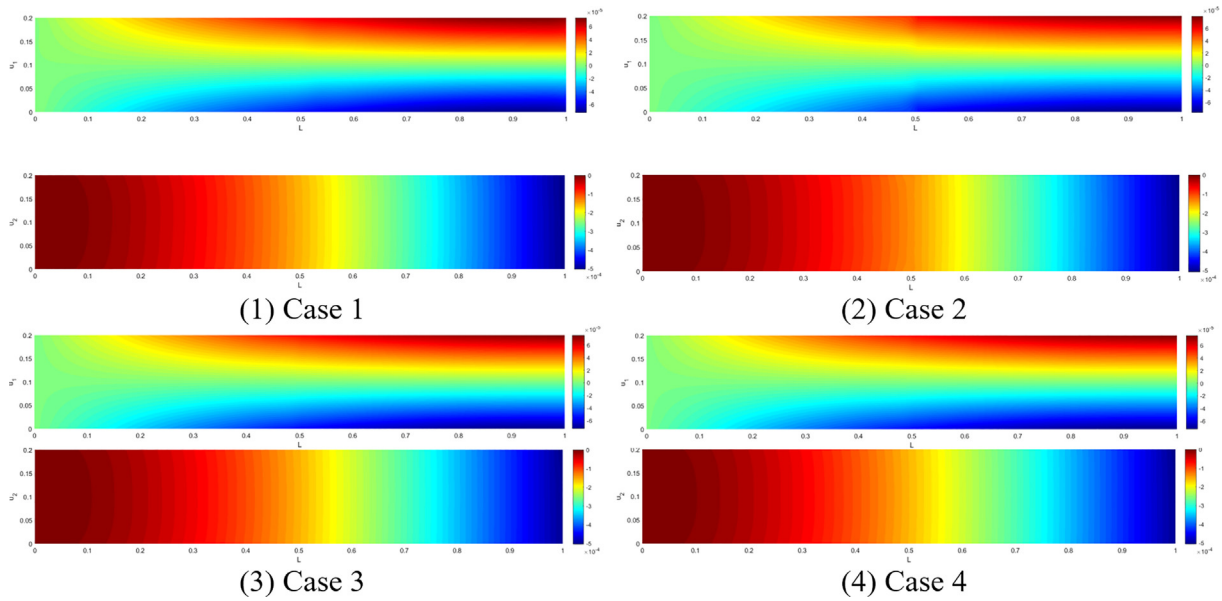

Fig. 14. Contour plots of the displacement u_1 and u_2.

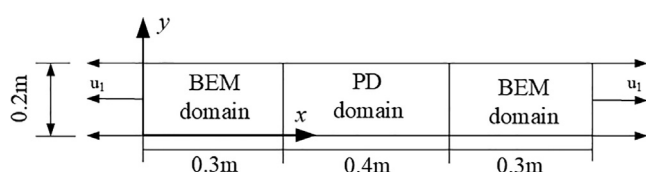

Fig. 15. Stretching of a 2D elastic domain.

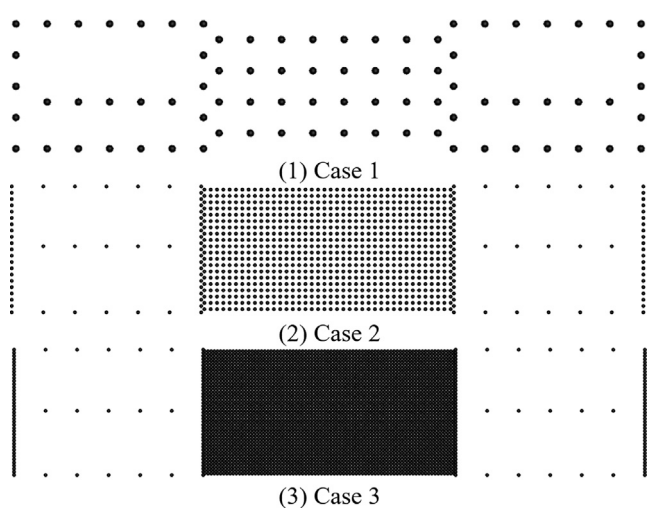

Fig. 16. Three BEM and PD domain discretization cases.

Table 4
Three discretization cases.

Cases	Numbers of BE and MP
Case 1	20 BE and 42 MP
Case 2	52 BE and 842 MP
Case 3	92 BE and 3282 MP

pling approach. In all the examples, a plane stress condition is assumed. Quadratic boundary elements are applied in the BEM domain, and in the PD domain, the horizon radius $\delta = 4\Delta x$.

Example 1:. *Mode I crack*

A plate with a central crack 10 mm in length is shown in Fig. 19. The Young's modulus is 30 GPa, and Poisson's ratio is 1/3. The plate is subjected to a displacement condition at the left and right ends, and the increment of the displacements for each step is 2.0e-8 m. The critical stretch s_c is 8.0e-4. For this example, the crack displacement direction is perpendicular to the propagation direction, which is called the Mode I crack. The plate is divided into three regions: the center is the PD domain with a material point spacing of Δx = 0.5 mm. Both sides are the BEM domains, the node distance at the edges near the PD domain is the same as the material point spacing, and the other two edges have a node distance equal to 2.5 mm.

After 278 increments (displacement loading is 5.56e−6 m), damage occurs at the crack tips. The corresponding displacement contours are plotted in Fig. 20, where the displacements are symmetrical with respect to the crack direction and continuous at the interface. The crack continued to propagate with increasing displacement loading, and the process of crack propagation is displayed in Fig. 21. The predicted crack propagation paths after 406 incremental steps (displacement loading is 8.12e−6 m) when the crack reaches the plate boundary, which as expected is in good agreement.

Example 2:. *Mixed-mode crack*

Mixed-mode cracks are the primary forms in practice. A mixed-mode I/II crack is obtained by rotating the crack in Example 1 by an inclination of 45°, as shown in Fig. 22. The geometry, loading, and discretization are the same as in Example 1. The displacement contours at 309 (displacement loading is 6.18e−6 m) steps when the crack tip damage begins and 381 steps are plotted in Fig. 23. With increasing displacement loading, the crack expands. Fig. 24 shows

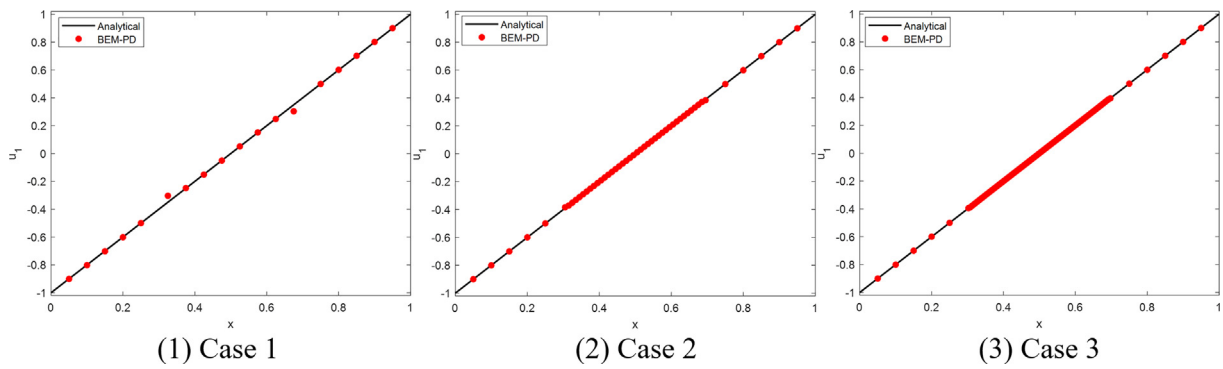

Fig. 17. Comparison the present results with the analytical solutions.

Table 5
Computing time and solution error for Example 3.

Cases	Numbers of BE and MP	Time (s)	Interface error (%)	Results error (%)
Case 1	20 BE and 42 MP	0.11	13.28	0.11
Case 2	52 BE and 842 MP	1.22	1.36	0.11
Case 3	92 BE and 3282 MP	8.92	0.19	0.00

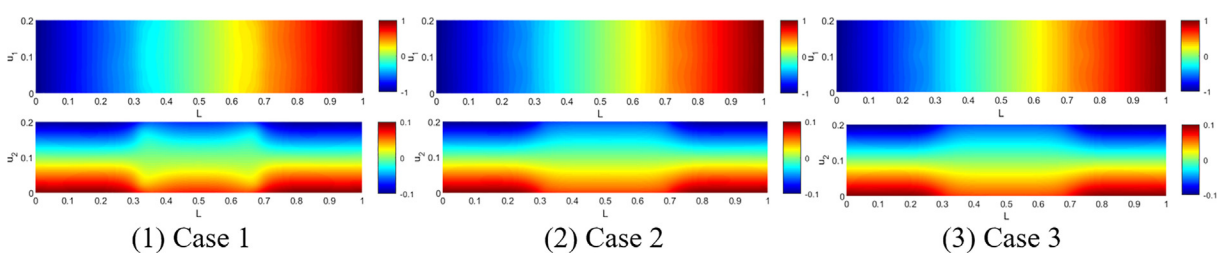

Fig. 18. Contour plots of the u_1 and u_2.

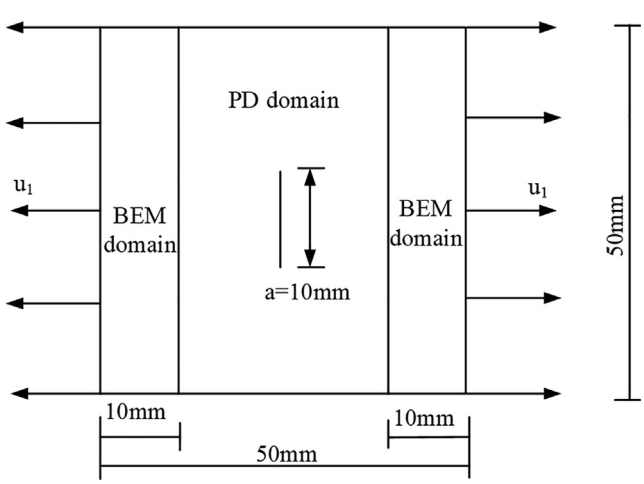

Fig. 19. A central crack model.

the crack propagation process. The predicted crack propagation paths after 454 (displacement loading is 9.08e−6 m) incremental steps when the crack reaches the plate boundary.

Example 3:. *Two-edge cracks*

In this example, a rectangular plate with two 2 mm long edge cracks, which are vertically offset by 2 mm on opposite sides, is considered in Fig. 25. A tension load is applied on the top of the plate, and an increment of 0.1 MPa is set for each step. The plate is supported at the bottom. The Young's modulus is 72 GPa, Poisson's ratio is 1/3, and fracture toughness is 3288.76 N/mm$^{1.5}$. The center is predicted by the PD domain with the material point spacing of Δx = 0.5 mm. The node distance at the left and right-side edges of the BEM domain is 2.5 mm. Fig. 26 shows the displacement contours and damage at 46 step increments (force loading is 4.6 MPa) when the crack tip damage occurs. The cracks propagate with increased force loading. Displacement contours and the corresponding damage after 78 increments are shown in Fig. 27. The crack propagation process is plotted in Fig. 28. Two cracks pass

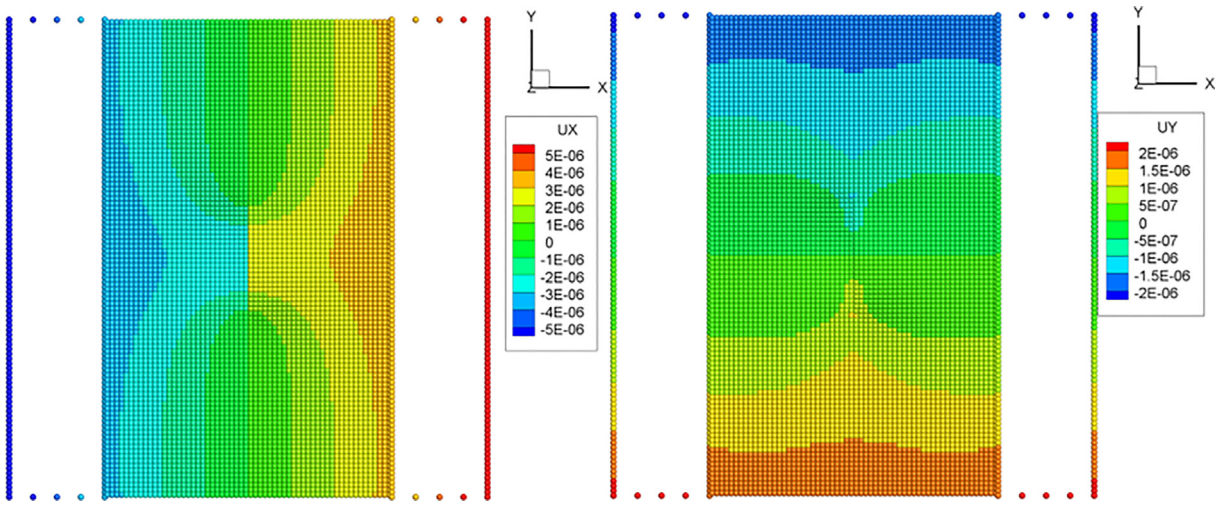

Fig. 20. Displacement contours of mode I crack.

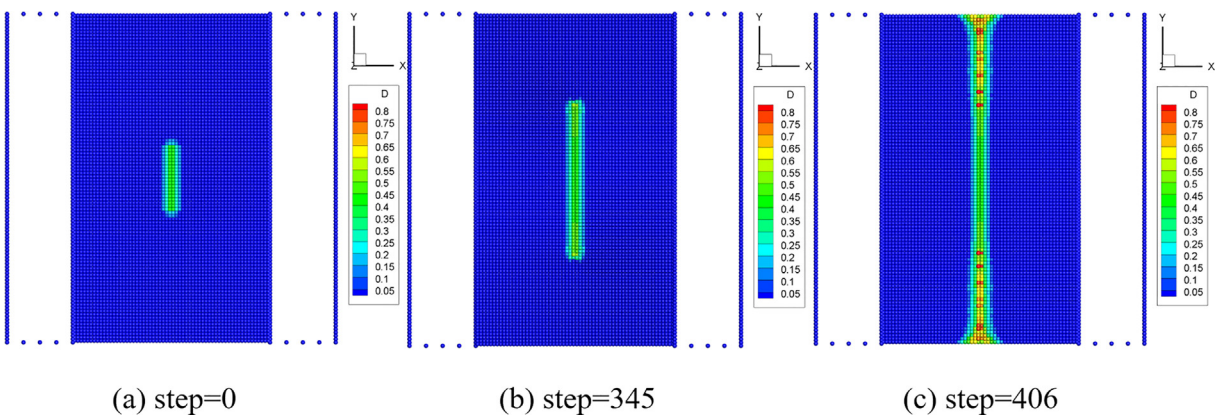

Fig. 21. Crack propagation process of mode I crack.

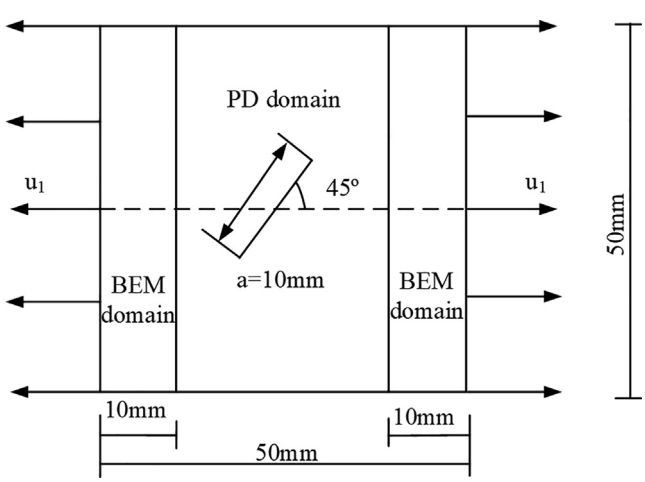

Fig. 22. A mixed mode crack model.

through the predicted propagation paths after 83 (force loading is 8.3 MPa) increments of the cracks. These results are consistent with results reported in the literature (Liu et al., 2017) or observed for similar cases.

5. Conclusions

In this study, a new multiscale method is developed by coupling the BEM and PD. The direct combination of these two methods produces a perfect match. The excellent performance of the coupling method is illustrated by several test examples with or without cracks. The following key conclusions can be drawn:

(1) A method with a full combination of the BEM and PD was first developed and studied.
(2) The high efficiency of BEM is designed to help offset the high computational cost of PD while maintaining good accuracy.
(3) The general stiffness matrix for the coupling model can be obtained by merging the stiffness matrix of the BEM and the stiffness matrix of the PD based on the continuity of displacements and equilibrium of tractions at the interface.

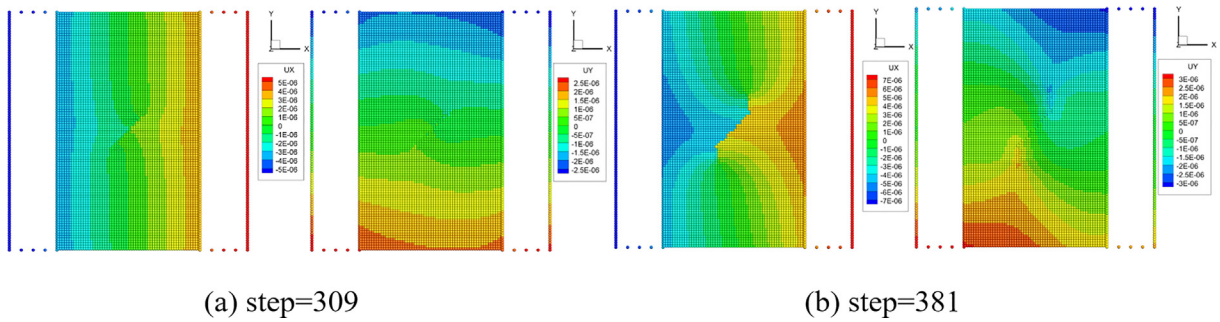

Fig. 23. Displacement contours of mixed-mode crack.

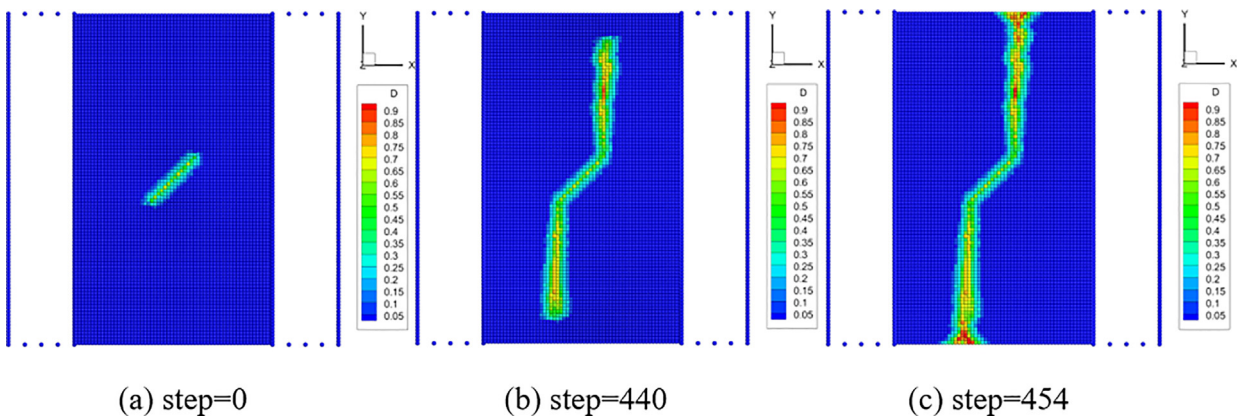

Fig. 24. Crack propagation process of mixed-mode crack.

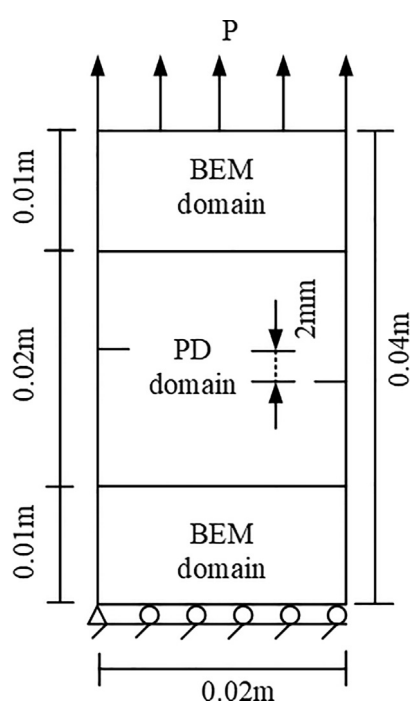

Fig. 25. A plate with two edge cracks.

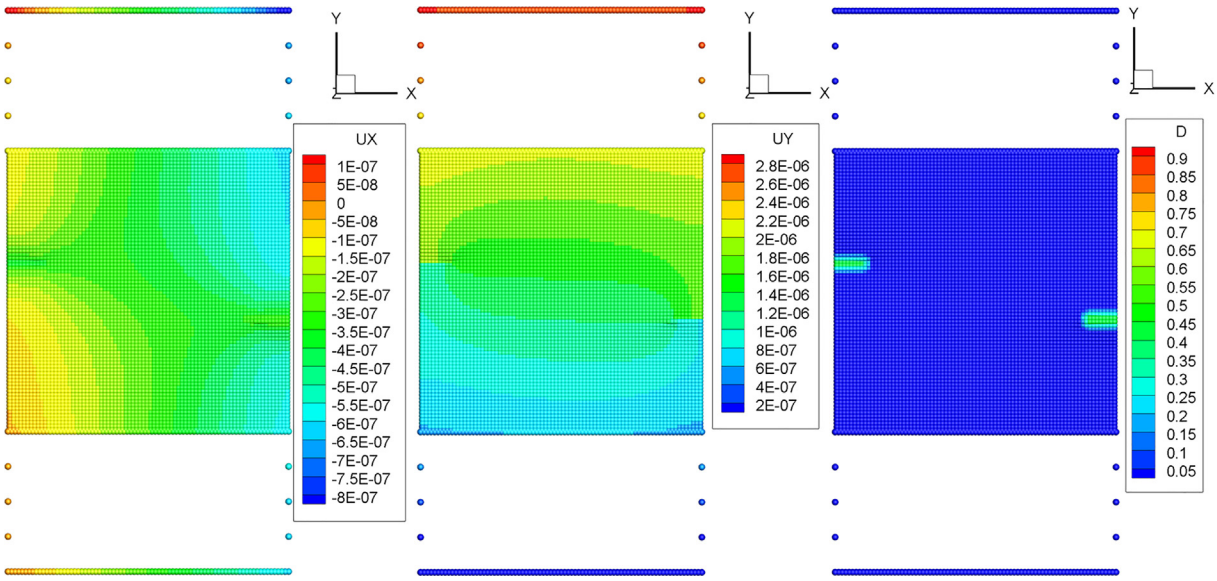

Fig. 26. Displacement contours and damage of Step 46.

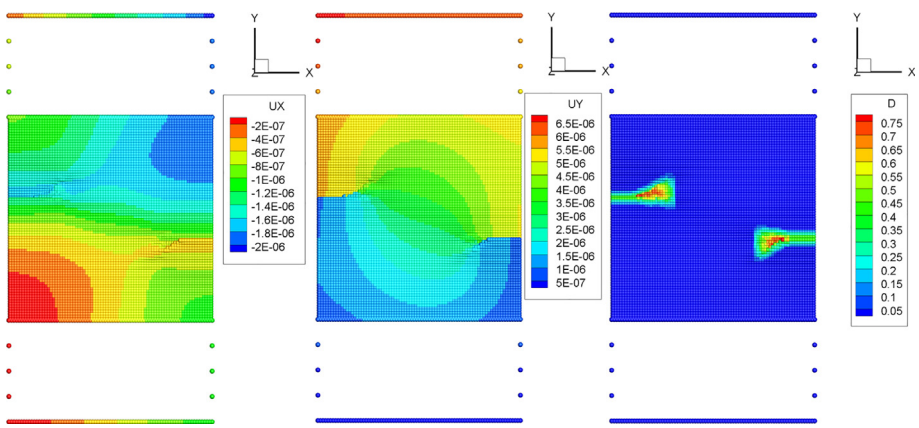

Fig. 27. Displacement contours and damage of Step 78.

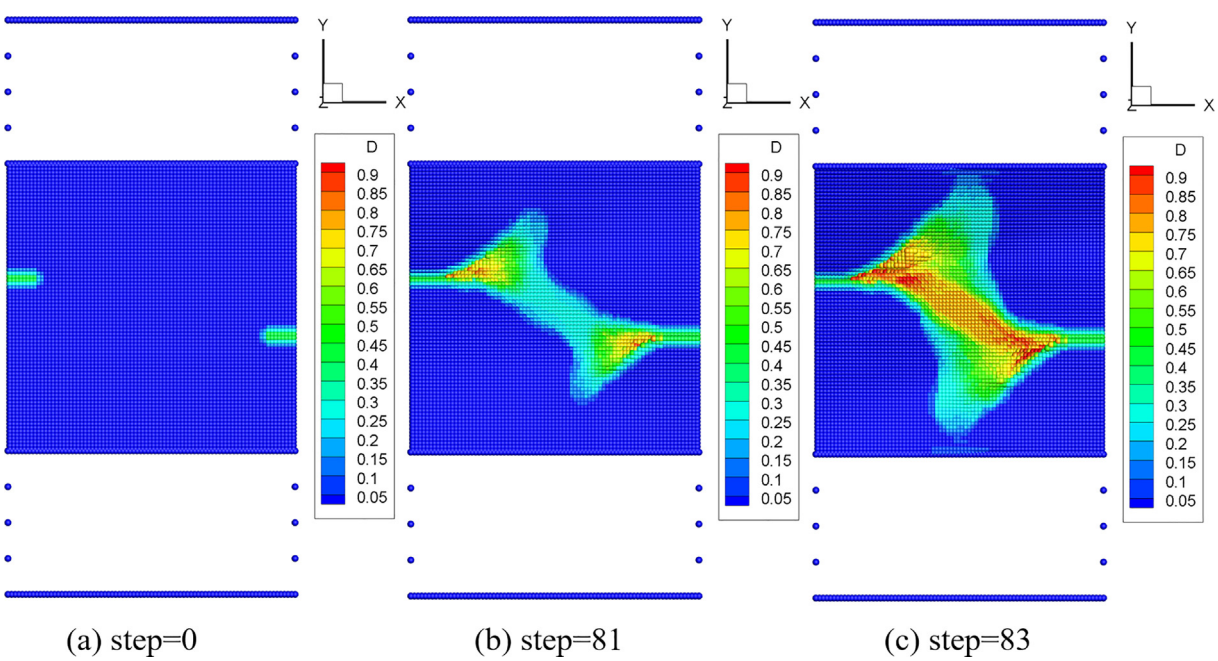

Fig. 28. Crack propagation process of two-edge cracks.

(4) The proposed sharing node coupling model avoids complex techniques such as mapping, morphing, and blending functions in transitional zone-based approaches.
(5) The node distance of BEM elements near the PD domain is the same as the PD material point spacing to ensure that the nodes in these BEM elements can be simultaneously regarded as PD material points.

The proposed coupling model accuracy can provide a precise tool for predicting the fracture process of brittle materials under static loading.

Declaration of Competing Interest

The authors declare that they have no known competing financial interests or personal relationships that could have appeared to influence the work reported in this paper.

Acknowledgements

The authors would like to acknowledge the funding of the National Natural Science Foundation of China (Project Nos. 11901283 and 11972179) and the China Postdoctoral Science Foundation Grant (Project No. 2019M662187) for supporting this research project.

References

Agrawal, S., Zheng, S., Foster, J.T., et al., 2020. Coupling of meshfree peridynamics with the Finite Volume Method for poroelastic problems. J. Petrol. Sci. Eng. 192, 107252.
Agwai, A., Guven, I., Madenci, E., 2012. Drop-shock failure prediction in electronic packages by using peridynamic theory. IEEE Trans. Compon. Packag. Manuf. Technol. 2, 439–447.
Belytschko, T., Black, T., 1999. Elastic crack growth in finite elements with minimal remeshing. Int. J. Numer. Meth. Eng. 45.
Dias, J.P., Bazani, M.A., Paschoalini, A.T., et al., 2017. A Review of Crack Propagation Modeling Using Peridynamics // Probabilistic Prognostics and Health Management of Energy Systems. Springer Int. Publ., 111–126
Galvanetto, U., Mudric, T., Shojaei, A., Zaccariotto, M., 2016. An effective way to couple FEM meshes and Peridynamics grids for the solution of static equilibrium problems. Mech. Res. Commun. 76, 14–47.
Giannakeas, I.N., Papathanasiou, T.K., Fallah, A.S., et al., 2020. Coupling XFEM and peridynamics for brittle fracture simulation—part I: feasibility and effectiveness. Comput. Mech. 66, 103–122.
Han, F., Lubineau, G., Azdoud, Y., et al., 2016. A morphing approach to couple state-based peridynamics with classical continuum mechanics. Comput. Methods Appl. Mech. Eng. 301, 336–358.
Han, D., Zhang, Y., Wang, Q., et al., 2019. The review of the bond-based peridynamics modeling. J. Micromech. Mole. Phys. 4, 1830001.
G. Hattori, and J. Trevelyan, An overview of the peridynamics (PD) formulation with the extended boundary element method (XBEM) for dynamic fracture, in 18th International Conference on Boundary Element Techniques: Bucharest, Romania, 11-13 July 2017; proceedings, pp. 64-70.
Huang, D., Lu, G., Wang, C., et al., 2015. An extended peridynamic approach for deformation and fracture analysis. Eng. Fract. Mech. 141, 196–211.
Kilic, B., Madenci, E., 2009. Coupling of peridynamic theory and the finite element method. J. Mech. Mater. Struct. 5, 707–733.
Kou, K.P., Yang, Y., 2019. A meshfree boundary-domain integral equation method for free vibration analysis of the functionally graded beams with open edged cracks. Compos. B Eng. 156, 303–309.
Lall, P., Shantaram, S., Panchagade, D., 2010. Peridynamic-models using finite elements for shock and vibration reliability of leadfree electronics. Thermal & Thermomechanical Phenomena in Electronic Systems, IEEE.
Liu, Y.J., 2009. Fast multipole boundary element method: theory and applications in engineering. Cambridge University Press, Cambridge.
W. Liu, J. W. Hong, A coupling approach of discretized peridynamics with finite element method. Computer Methods in Applied Mechanics and Engineering, s245–246 (2012), 163–175.
Liu, S., Fang, G.D., Liang, J., et al., 2020. A coupling model of XFEM/peridynamics for 2D dynamic crack propagation and branching problems. Theor. Appl. Fract. Mech. 108, 102573.
Liu, Y.J., Li, Y.X., Xie, W., 2017. Modeling of multiple crack propagation in 2-D elastic solids by the fast multipole boundary element method. Eng. Fract. Mech. 172, 1–16.
Lubineau, G., Azdoud, Y., Han, F., et al., 2012. A morphing strategy to couple non-local to local continuum mechanics. J. Mech. Phys. Solids 60, 1088–1102.
Macek, R.W., Silling, S.A., 2007. Peridynamics via finite element analysis. Finite Elem. Anal. Des. 43, 1169–1178.
Madenci, E., Oterkus, E., 2014. Peridynamic Theory and Its Applications. https://doi.org/10.1007/978-1-4614-8465-3.
Moës Nicolas, J., Dolbow, T.B., 1999. A finite element method for crack growth without remeshing. Int. J. Numer. Meth. Eng. 46, 131–150.
Nikpayam, J., Kouchakzadeh, M.A., 2019. A variable horizon method for coupling meshfree peridynamics to FEM. Comput. Methods Appl. Mech. Eng. 355, 308–322.
Nishioka, T., 1997. Computational dynamic fracture mechanics. Int. J. Fract. 86, 127–159.
Oterkus, E., Madenci, E., Weckner, O., et al., 2012. Combined finite element and peridynamic analyses for predicting failure in a stiffened composite curved panel with a central slot. Compos. Struct. 94, 839–850.
Qiao, P.Z., Zhang, Y., Zhang, H., et al., 2017. A review on advances in peridynamics. Chin. Quarter. Mech. 38, 1–13.
Seleson, P., Beneddine, S., Prudhomme, S., 2013. A force-based coupling scheme for peridynamics and classical elasticity. Comput. Mater. Sci. 66, 34–49.
Silling, S.A., 2000. Reformulation of elasticity theory for discontinuities and long-range forces. J. Mech. Phys. Solids 48, 175–209.
Silling, S.A., Epton, M., Weckner, O., et al., 2007. Peridynamic States and Constitutive Modeling. J. Elast. 88, 151–184.
Silling, S.A., Lehoucq, R.B., 2010. Peridynamic Theory of Solid Mechanics. Adv. Appl. Mech. 44, 73–168.
Yu, Y.T., 2017. Hybrid modeling methods of peridynamics and finite element method Master thesis. Ho Hai University.
Zaccariotto, M., Tomasi, D., Galvanetto, U., 2017. An enhanced coupling of PD grids to FE meshes. Mech. Res. Commun. 84, 125–135.
Zaccariotto, M., Mudric, T., Tomasi, D., et al., 2017. Coupling of FEM meshes with Peridynamic grids. Comput. Methods Appl. Mech. Eng. S0045782516318886.
Zeng, Z., Su, Y.C., Zhang, X., et al., 2020. Combining peridynamics and generalized interpolation material point method via volume modification for simulating transient responses. Comput. Particle Mech., 1–11
Q. Zhang, Y. T. Yu, X. Gu, Hybrid modeling methods of peridynamics and finite element method. Chinese Journal of Computational Mechanics, 33 (2016), 441-448+450.
Zheng, G., Shen, G., Hu, P., et al., 2020. Coupling approach of isogeometric analysis with non-ordinary state-based peridynamics. Eur. J. Mech. A Solids 82, 103981.